Zhang *et al. Soft Sci.* **2025**, *5*, 15
DOI: 10.20517/ss.2024.71

Soft Science

Research Article

Open Access

Photothermal-driven water-gliding microrobots based on fully integrated flexible sensors with heterogeneous wettability

Zhixing Zhang[1,2], Neng Gao[1,3], Fei Zhang[1], Lanlan Liu[1], Ying Chen[1,*]

[1]Institute of Flexible Electronics Technology of THU, Zhejiang, Jiaxing 314000, Zhejiang, China.
[2]School of Materials Science and Engineering, Tianjin University, Tianjin 300354, China.
[3]School of Materials and Energy, University of Electronic Science and Technology of China, Chengdu 610054, Sichuan, China.

[*]**Correspondence to:** Dr. Ying Chen, Institute of Flexible Electronics Technology of THU, No.40, HuaChuang Road, Jiaxing 314000, Zhejiang, China, E-mail: chenying@ifet-tsinghua.org

How to cite this article: Zhang, Z.; Gao, N.; Zhang, F.; Liu, L.; Chen, Y. Photothermal-driven water-gliding microrobots based on fully integrated flexible sensors with heterogeneous wettability. *Soft Sci.* **2025**, *5*, 15. https://dx.doi.org/10.20517/ss.2024.71

Received: 6 Dec 2024 **First Decision:** 30 Dec 2024 **Revised:** 10 Jan 2025 **Accepted:** 21 Jan 2025 **Published:** 22 Feb 2025

Academic Editor: YongAn Huang **Copy Editor:** Pei-Yun Wang **Production Editor:** Pei-Yun Wang

Abstract

Bionic water strider robots (BWSRs) have been a hot spot in research due to their unique biological inspiration and versatile applications in environmental monitoring. However, creating aquatic micro-robots with combined structure and function that can walk freely and perceive environmental information on water surfaces remains a challenge. Herein, self-propelled and integrated aquatic microrobots that can be remotely controlled by light and wireless environment detection are designed and fabricated by combining the actuating polydimethylsiloxane (PDMS)/carbon nanotube (CNT) substrate with heterogeneous wettability and the fully integrated wireless sensors. The substrate generates thrust on water through the photothermal Marangoni effect, serving as the propulsion system for this water-gliding microrobot. The heterogeneous wettability design features the robot with a hydrophobic body and four hydrophilic footpads. The hydrophobic body creates an air gap between the device and water, providing waterproof protection for electronics, making the robot move faster with smaller power and enabling greater load-carrying capacity. The hydrophilic footpads help the robot stand firmly on water, resisting overturn by waves and also enable modular assembly between robots. The load ability of a typical robot is 1,089% of its weight, resulting in the manufacture of microrobots with fully integrated visible light sensors and Bluetooth (BT) chips that can be steered by near-infrared laser. Hopefully, this strategy shall help to develop untethered aquatic robots with sophisticated actuation and wireless sensing for complex aquatic environments.

Keywords: Water-gliding microrobots, photothermal Marangoni effect, self-propelled actuator, wireless sensing, heterogeneous wettability

INTRODUCTION

Natural creatures with biologically evolved unique structures always inspire us to develop advanced systems and robots[1-3]. The water strider is a long-legged inset that can effortlessly stand and sprint on the water surface at an average velocity of 60 body lengths per second[4]. To mimic the agile movement of water striders on water surfaces, bionic water strider robots (BWSRs) have been developed with an emphasis on their ability to remain and propel themselves[4-8]. After achieving floating on the water surface by the hydrophobic interfaces of surface-water robots, enabling them to move at high speeds and carry loads has become a widely recognized research hotspot. According to the movement of water strider's leg on the water surface, most BWSRs use mobile parts to beat the water surface to obtain the driving force. Moreover, various steering actuators have been utilized, such as shape memory alloys, ionic polymer-metal composites, Marangoni actuators and conventional motors[9-14]. However, as people pay growing attention to maritime rights and interests, the collection of water-related information becomes more crucial. This necessitates that aquatic robots possess capabilities in information perception, data processing, and transmission. As a type of aquatic robot, the BWSR is characterized by its small size. However, it faces challenges in performing water surface environment detection due to the lack of integrated sensing systems.

Sensing systems based on traditional rigid semiconductors have been widely used commercially because of their high technical maturity. Their large volume and heavy mass make them suitable for rigid robots but may cause interface mismatches when coupled with soft robots, leading to the failure of integrated systems. The intrinsic limitation of rigid electronics prohibits their integration in a flexible, lightweight, and compact fashion, which is extremely desirable for soft micro-robots. In contrast, the emerging flexible electronics demonstrate soft, small, and thin, which is very suitable for the structure of micro-robots, and promotes the multi-function integration of micro-bionic robots[15-17]. In recent years, various highly integrated micro-bionic robots have emerged, such as wind-dispersal dandelion microfliers, octopus robots, and flapping-wing microscale aerial vehicles[18-20]. In particular, the structure-function integration manufacturing, that is, integrating electronic systems and robot substrates in materials and structures, further promotes the miniaturization and functionalization of bionic robots, which inspired our research on BWSR. However, the key difficulty of manufacturing integrated BWSRs based on flexible electronic systems is the compact integrated design of structure and function. The goal of this design is to pursue structural lightweight, high functional integration, and maintain the floating stability of BWSRs in complex surface environments (current, wind, waves, *etc.*).

Herein, this work reports the facile fabrication of a photothermal-driven water-gliding BWSR based on fully integrated flexible sensors with heterogeneous wettability. As shown in Figure 1, the BWSR is designed as a three-layer structure by utilizing polydimethylsiloxane (PDMS) as the substrate for the actuator and the encapsulation layer for the wireless sensing platform. PDMS is well known as an excellent packaging material for electronic devices and is easy to compound with other materials. The obtained PDMS/carbon nanotube (CNT) with photothermal conversion is selectively designed as a four-legged structure, forming a heterogeneous wettable surface with superhydrophobicity in the middle and hydrophily around. This results in an air gap at the solid-liquid interface in the central area of the BWSR, which helps to isolate the erosion of the circuit by liquid water and improves the robot's floating stability. Based on photothermal Marangoni effect, the obtained robot can walk freely on the water under near-infrared light irradiation, revealing great potential for cutting-edge applications in environment monitoring.

EXPERIMENTAL

Preparation of the floating device

The devices were fabricated using a commercially available PDMS elastomer (Sylgard 184 Silicone

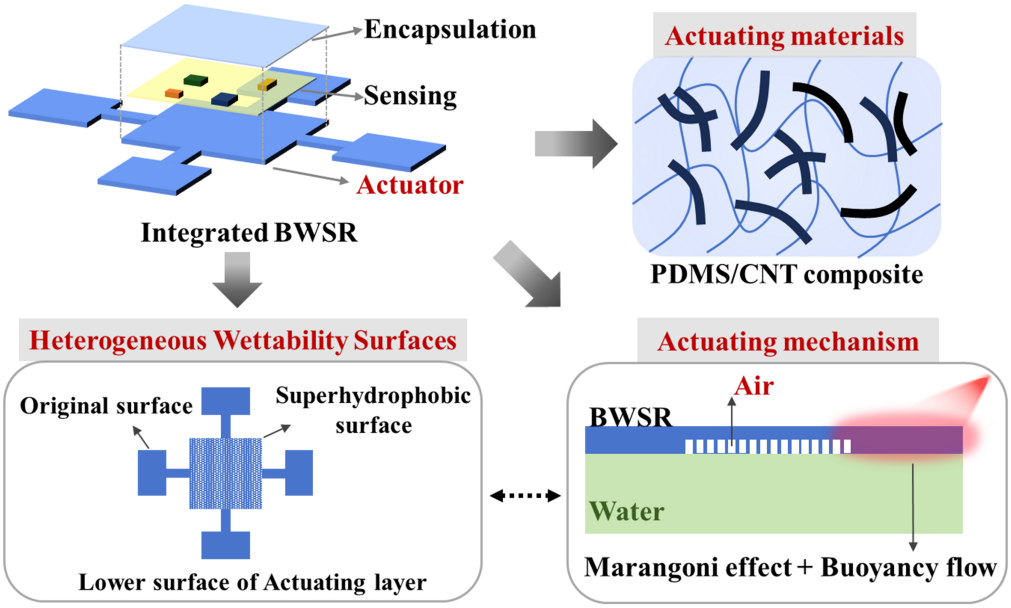

Figure 1. A schematic illustration of the structure of the integrated BWSR in this work. The microrobot is composed of an actuating layer, a sensing layer and an encapsulating layer. The PDMS/CNT composite is the basis for micro-robots to realize water surface sliding based on the photothermal effect. The propulsion force is generated by the Marangoni effect and buoyancy flow, which are created by the laser local heating actuating layer. The reasonably designed solid-liquid interface structure of the actuator provides conditions for robot integration. BWSR: Bionic water strider robot; PDMS: polydimethylsiloxane; CNT: carbon nanotube.

Elastomer, Dow Corning Corporation) and CNTs (XFM13, Nanjing XFNANO Materials Tech Co., Ltd). Typically, a PDMS prepolymer was mixed with a curing agent (10:1 by weight) and CNTs (5 wt%), and then a membrane with a thickness of about 200 μm was prepared after the curing process at 80 °C for 2 h. A carbon dioxide laser engraving machine [DL300U, DCT(Tianjin) Direct Laser Technology Co., Ltd.] was used to pattern the device with programmable shapes and to separate it from the base materials. Then, the patterned PDMS composite was laser-treated for surface modification. The laser scanning speed is 200 mm/s and the fabrication efficiency is 50 kHz.

The Bluetooth (BT) wireless transmission sensing system is customized with surface-mounted electronic components [Such as: Ambient light sensor, PT19-315C (Everlight); Bluetooth chip, PAN102 (Panchip); Digital conversion chip, MS1112 (Relom)]. An integrated actuator can be obtained by encapsulating the customized circuit board on a prefabricated PDMS/CNT film using PDMS. The following is a brief description of the preparation process. First, the circuit board is placed in the middle area of the actuator. The PDMS prepolymer is then poured onto the circuit board to make it fully coated. After the PDMS is cured, an actuator loaded with a wireless sensing system can be obtained.

Characterization

Scanning electron microscopy (SEM) images were obtained using a field emission scanning electron microscope (Sirion 200, FEI). A digital microscope (VHX-5000) was used to observe the 3D microscopic morphology of the samples. The contact angle measurements were conducted using a contact angle meter (JY-82C, Dingsheng Tech. Chengde). Thermal images were obtained using an infrared thermal camera (226s, FOTRIC). The laser used in this study was a handheld infrared laser with a center wavelength of 808 nm and tunable energy density, a model of MDL-SN-808-12W. A white light-emitting diode (LED) light (Bull, China) is used to create ambient light, and the light intensity is calibrated using an illuminometer (1801C, DELIXI).

RESULTS AND DISCUSSION

Design and fabrication

To achieve the photo-response actuating material, the typical soft PDMS was used as the matrix, and CNTs with a length of approximately 20 μm were used as the additive. The required materials were synthesized and the structures of actuators were tailored, as shown in Figure 2A, which shows the preparation diagram of actuators. Firstly, an uncured composite solution with a uniform mixture of PDMS, curing agent, and CNTs was prepared. Then, the composite solution was poured into the template, blade-coated, heated, and solidified for a certain period to obtain the PDMS/CNT composite films. Finally, patterns on different scales were produced by laser engraving technology. By controlling the power of the laser and the scanning path, a concave-convex microstructure can be formed on the surface of the composite film. As shown in the SEM images [Figure 2A(i) and (ii)], ablation grooves were formed on the PDMS/CNT surface, surrounded by redeposition areas. Moreover, the rough surface is also shown in 3D optical photographs [Supplementary Figure 1]. When the laser power is large enough, the laser can burn through the film, and macroscopic samples with various shapes can be obtained by designing the laser path, such as round, square, and polygon [Figure 2A(iii)]. Importantly, the resulting microstructure shows significant superhydrophobicity. In Figure 2B, the water drops form a large contact angle on the rough film surface. At the same time, the water droplets can easily leave the material surface, indicating that this rough structure has superhydrophobicity and low adhesion. More comparative experimental results are shown in Supplementary Figure 2. At any tilt angle, the water droplet can adhere to the surface of the uncarved material, but on the carved rough surface, the water droplet can easily slide away. According to the water contact angle tester, the water contact angle of this rough surface is about 160°, and the rolling angle is less than 1°. In comparison, the water contact angle on the initially uncarved surface of the film is 89°. The significant change in membrane surface wettability after structural modification provides a basis for subsequent research on the motion performance of actuators.

Self-propulsion of the floating actuator

In this section, a square actuator (10 mm × 10 mm) was used to verify the effect of the solid-liquid interface on sliding motion performance. Figure 3A shows the motion phenomenon of a typical actuator based on the photothermal Marangoni effect. Under near-infrared light irradiation, the film actuator is heated based on the photothermal conversion effect of CNTs. The high-temperature film transfers heat to the low-temperature liquid at the solid-liquid interface, resulting in differences in surface tension around the film. Then the film actuator slides on water by exploiting the propulsive force (F_d) generated by surface tension differences. Furthermore, given the significant influence of rough microstructure on the wettability of membrane materials, the sliding behavior of actuators with different solid-liquid interfaces is investigated. Figure 3B and C shows the statistical results of sliding behavior parameters of wetted samples and non-wetted samples, respectively. Response time is the time for accumulated irradiation before the actuator slips, and sliding velocity refers to the average speed after the actuator starts moving. Obviously, for the original sample [Figure 3B], when the laser power density is low (< 0.6 W/cm^2), the actuator needs a longer excitation time. As the laser power density increases, the response time gradually decreases, which is determined by the photothermal conversion characteristics of the actuating material. The longer the illumination time, the greater the light power and the higher the temperature of the sample [Supplementary Figure 3]. Although the superhydrophobic sample also shows a similar phenomenon, the response time of the superhydrophobic sample is less than that of the original sample under the same irradiation condition [Figure 3C]. Moreover, both the superhydrophobic and original samples require high-power illumination to achieve maximum gliding speed. This phenomenon can be explained by the Marangoni-driven flow, which generally occurs at a liquid-air or liquid-liquid interface[21]. At the solid-liquid interface, buoyancy flow predominates, with Marangoni flow playing a secondary role. Superhydrophobic surfaces provide the necessary liquid-air interface to trigger evident Marangoni flows. When the superhydrophobic sample is

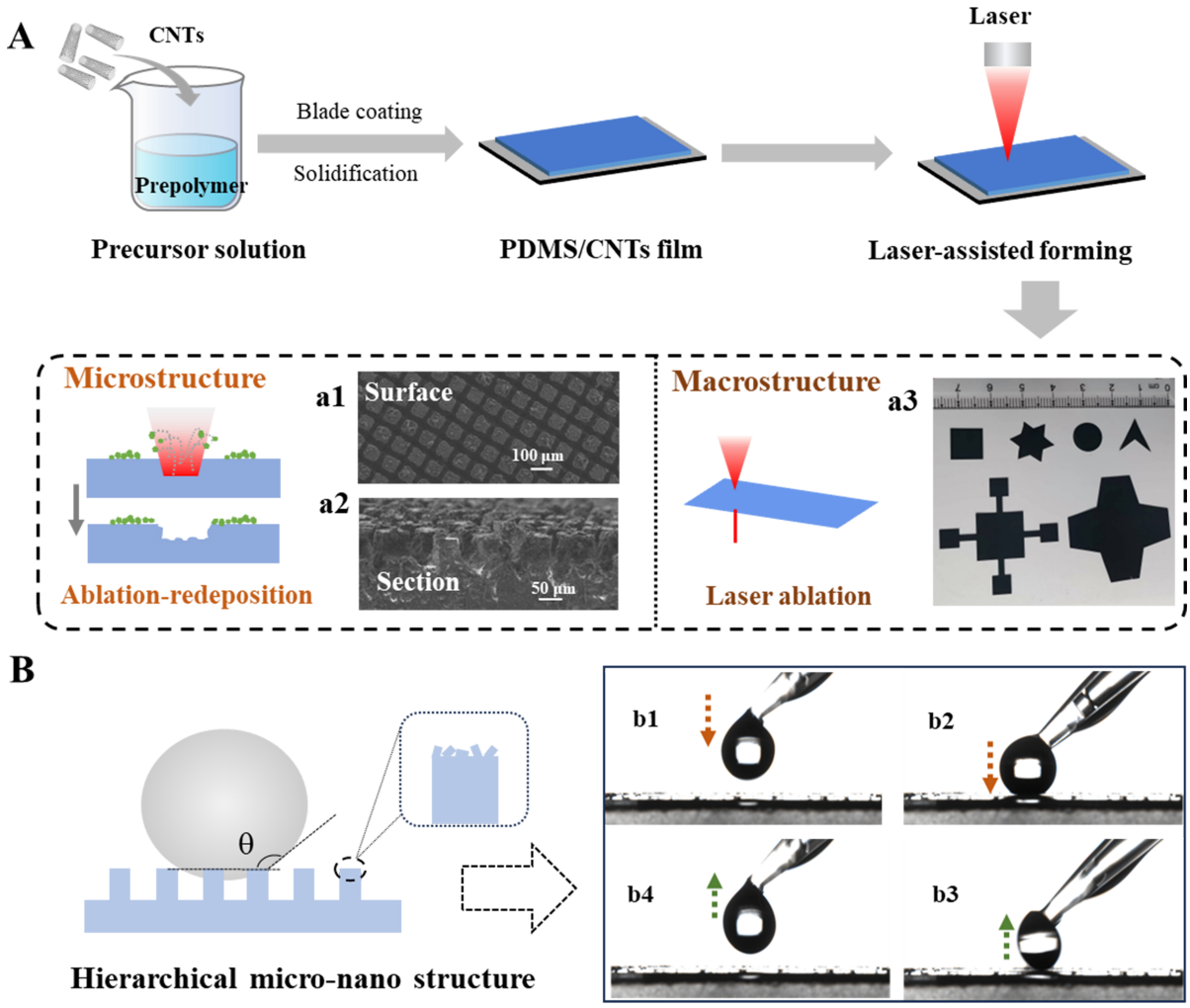

Figure 2. (A) Diagram of the preparation process of photothermal PDMS/CNT composites with different structure; These inserted SEMs show the surface (i) and section (ii) structures of the carved sample. The picture (iii) shows macroscopic samples of various sizes; (B) Schematic of the superhydrophobic structure and superhydrophobic phenomenon of PDMS/CNT composite showing that a drop of water does not adhere to the material surface. θ is the water contact angle. PDMS: Polydimethylsiloxane; CNT: carbon nanotube; SEMs: scanning electron microscopes.

locally heated with a laser, the very small solid-liquid contact area allows for rapid heating of the liquid, forming a significant temperature gradient between the liquid and its surrounding environment. This leads to a significant Marangoni flow in a short time. In contrast, for the original sample, the larger solid-liquid contact area results in a more uniform photothermal distribution, causing slower liquid heating. It takes longer to accumulate sufficient heat to produce a large temperature difference, which generates more significant buoyancy flow.

To better comprehend the effect of the solid-liquid interface structure on the motion performance of the actuator, a schematic diagram is shown in Figure 3D. The actuator is known to be driven by the photothermal-induced Marangoni effect, which is related to the liquid surface tension. According to the Harkins formula and the temperature rise range (< 100 °C)[22], the surface tension was calculated using

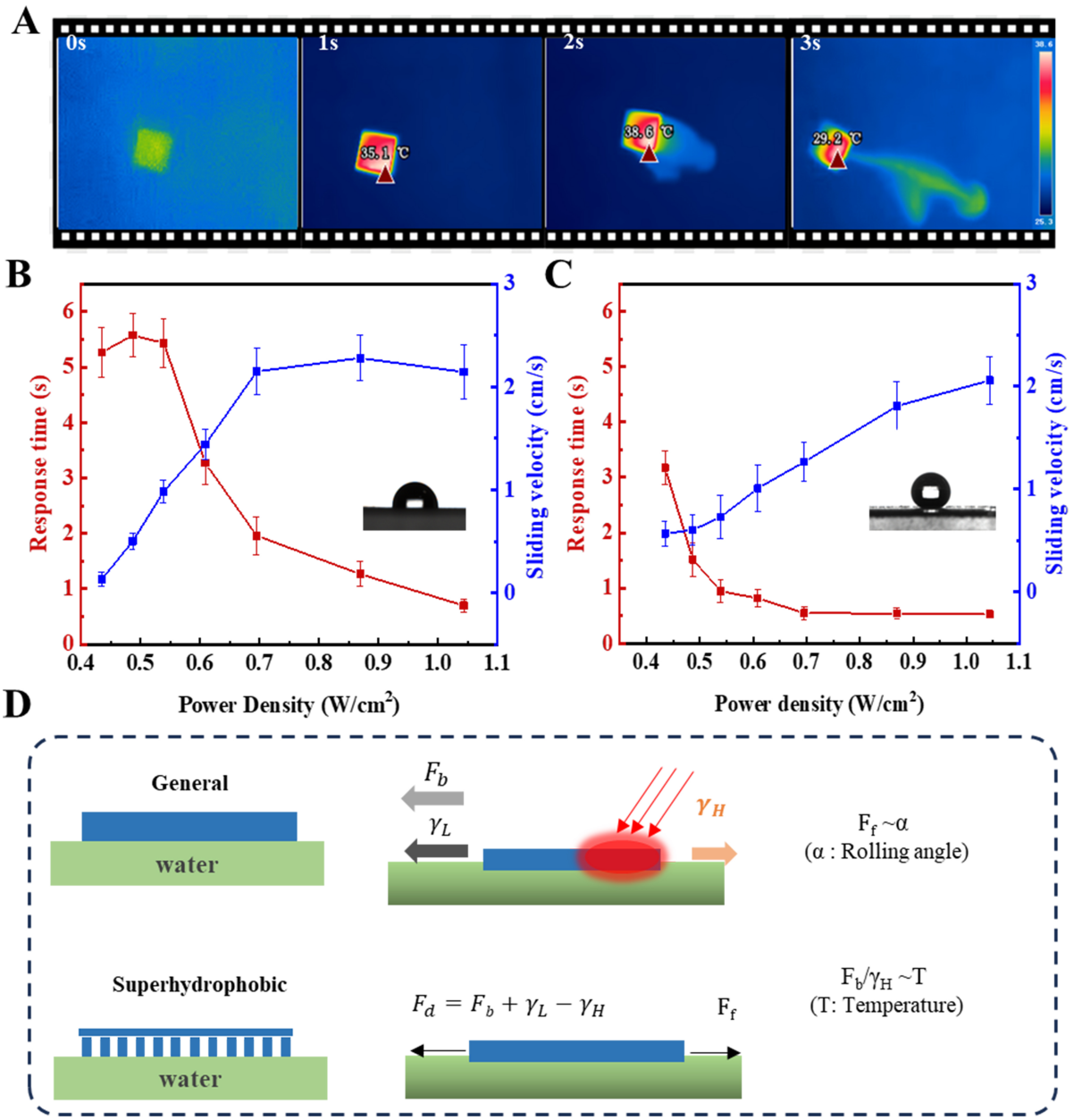

Figure 3. (A) Thermography images of the movement of the light-driving actuator at different time points; (B) Relationship between driving characteristic and light intensity of actuator with the original surface; (C) Relationship between driving characteristic and light intensity of actuator with superhydrophobic surface; (D) Schematic of actuator with different surface structures based on Marangoni effect. γ_L is the surface tension with low temperature. γ_H is the surface tension with high temperature. F_b is a propulsive force caused by a buoyant flow. F_d is the resultant propulsive force. F_f is the friction resistance.

$$\gamma = b_0 + b_1 T + b_2 T^2 \quad (1)$$

where γ is the surface tension, b is a constant term (b_0 = 75.796 mN·m^{-1}, b_1 = -0.145 mN·m^{-1}·°C^{-1}, b_2 = -0.00024 mN·m^{-1}·°C^{-2}), and T is the temperature; the surface tension of water is inversely proportional to the temperature. According to this mechanism, the higher the temperature, the lower the surface tension (γ_H) of the water. When the asymmetric temperature field of the water surface under light irradiation is

more significant, the tension difference (γ_L-γ_H) formed is larger, which leads to a large F_d. Moreover, the heated liquid can also produce a F_b caused by a buoyant flow. At the same time, the actuator would suffer friction resistance (F_f) when sliding, which is related to the structure of the solid-liquid interface. For the original sample, the solid and liquid are in complete contact at the interface, while for the superhydrophobic sample with convex and convex microstructure, the solid-liquid interface is composed of both solid-liquid contact and gas-liquid contact. The Cassie-Baxter formula is written as[23,24]:

$$cos\theta_c = \frac{f_1(\gamma_{sg}-\gamma_{sl})}{\gamma_{lg}} - f_2 = f_1 cos\theta - f_2 \quad (2)$$

where θ_c and θ are the apparent and intrinsic contact angles of droplets placed on rough surface and homogeneous smooth surface, respectively. f_1 and f_2 are the percentages of the solid-liquid contact surface and gas-liquid contact surface in the entire composite contact surface, and $f_1 + f_2 = 1$. In this study, it is calculated that the solid-liquid contact area is only about 3% for the superhydrophobic interface, meaning that the F_f of the rough surface is very small. The superhydrophobic sample, therefore, necessitates a brief response time to generate sufficient F_d for overcoming frictional resistance and achieving propulsion. However, compared with the original sample with a long response time under the same lighting conditions, the moving speed of the superhydrophobic sample would be lower. Moreover, the Janus wettability of the material affects the stability of the actuator on the surface of water. No matter in what direction the floater was incorporated on the water surface, it will automatically rotate to its normal orientation; that is, the superhydrophobic part is upward and the hydrophilic part is downward [Supplementary Figure 4]. This self-regulated floating ability is attributed to the wettability difference between superhydrophobic surface and wetted surface[25]. Accordingly, an actuator with different surface structures is designed and manufactured. The detailed structural parameters of the unconventional actuator are shown in Supplementary Figure 5.

The actuator is typically characterized by central symmetry, with superhydrophobic surfaces in their central regions. During the underwater floating process, this actuator can keep its superhydrophobic surface always located at the solid-liquid interface [Supplementary Figure 6]. To analyze the influence of the device structure on the motion characteristics, the irradiated region of the actuator was shaped in different sizes. As shown in Figure 4, we designed three types of actuators with different structures, the total area of which is unchanged while the shape of the irradiated region is changed, including roundness, triangle, and rectangular. As illustrated in the first two rows of Figure 4A, the actuators with different shapes are activated by directional irradiation of the photo-response area. The trajectory of the representative locations on the actuator is recorded in the third row in Figure 4A. Only the actuator of which the photo-response region is rectangular exhibits linear motion, while the rest exhibits rotational motion. For the actuator with rotational motion, the motion directions of the recording points A and B are opposite, and the rotational radius of A is significantly larger than that of B. When the actuator is placed on the water surface, the force of the microrobot is shown in the fourth row in Figure 4A.

The actuator was mainly subjected to gravity (G), water support force (F_N), and surface tension. When the infrared light irradiates the left side of the actuator, the surface tension on the left side of the actuator decreases, and the resultant force of the surface tension. Therefore, the resultant force (F) can be formulated as:

$$\vec{F} = \overrightarrow{\gamma_L} - \overrightarrow{\gamma_H} - \overrightarrow{F_f} \quad (3)$$

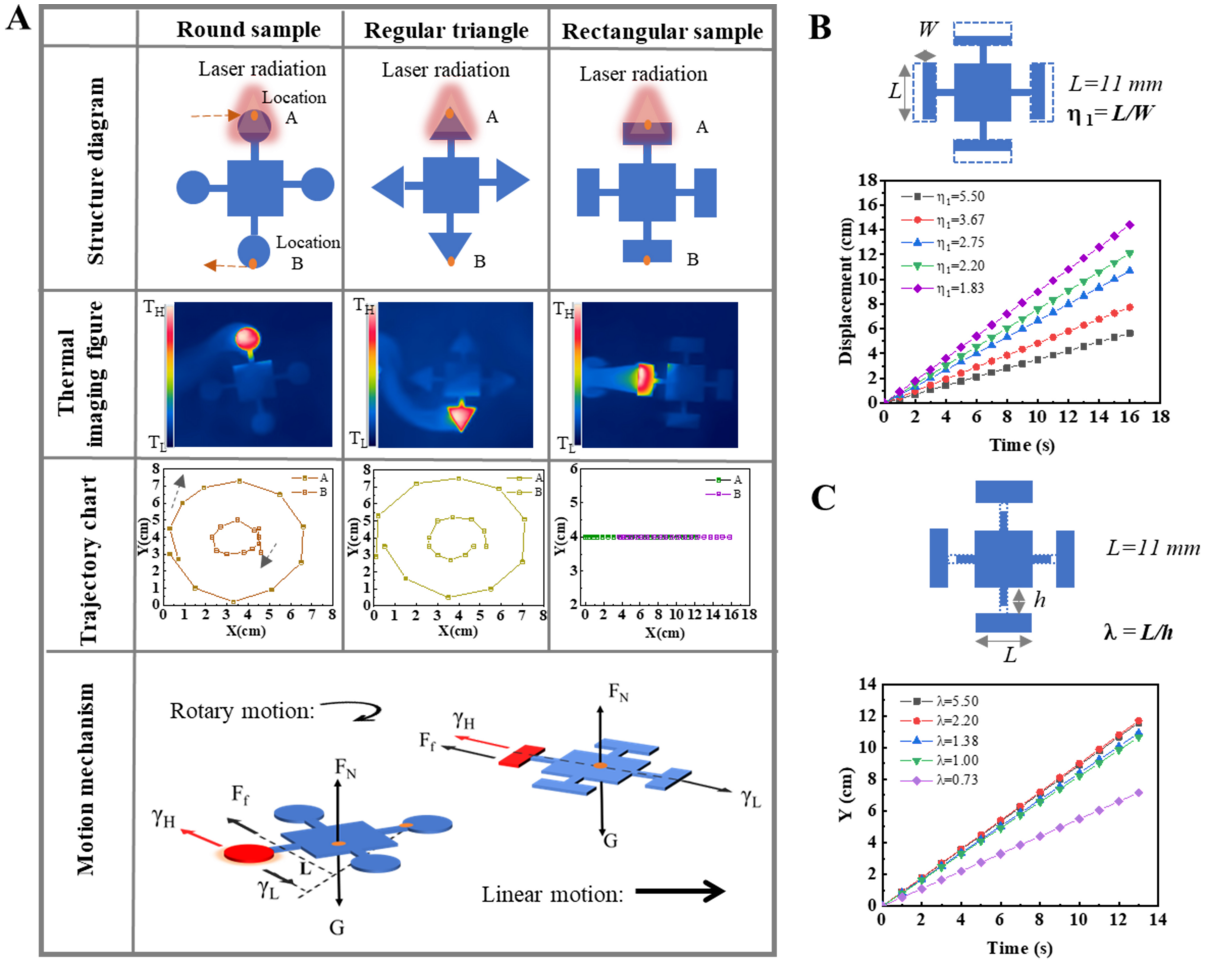

Figure 4. (A) Structure diagram, thermal imaging, trajectory and mechanism of actuators with irradiated region of the same area and different shapes. F_N is buoyancy. G is gravity. The distance between the resultant force and the axis of the actuators is L. Schematic and motion trajectory of the actuator with adjustable rectangular irradiated region: (B) adjustable length-width ratio (η_1) with the constant length and (C) adjustable length- distance ratio (λ) with the constant length.

where γ_H is the surface tension after infrared irradiation, and γ_L is the surface tension without irradiation. Once the resultant force of the surface tension intersects the center of gravity of the actuator, the actuator will move in a straight line. For these actuators with roundness structures, or triangle structures, when the infrared laser irradiates, the surface tension decreases, and the resultant force of the surface tension does not intersect with the center of gravity. The distance between the resultant force and the axis of the actuators is *L*. Therefore, a torque *T* is generated on the actuator, which causes these actuators to rotate. Notably, the rotation direction of the actuator is random. Clockwise or counterclockwise rotation of the actuator occurs depending on the initial resultant force direction formed when the laser begins to irradiate. Moreover, because of the continuous irradiation of the infrared laser, the actuator can realize fast and continuous rotation. Ultimately, the different motion forms of these actuators can be attributed to the coupling of the size of the laser spot and the irradiated region. As illustrated in the second row of Figure 4A, the resulting high-temperature regions (T_H) overlapped with the irradiated regions of the circle, and triangle, resulting in the rotational motion of the actuator. However, the irradiated regions of the rectangle only partially formed at high temperatures, which causes linear motion of the actuator.

To further investigate the influence of the irradiated region on the motion pattern of the actuator, the size of the rectangular irradiated region was adjusted, and the corresponding actuators exhibited different motion characteristics under the action of an infrared laser. As shown in Supplementary Figure 7A, the width of the radiation region is a fixed constant (W = 6 mm), and its length is adjusted to obtain actuators with different sizes. When the length is less than 10 mm, the actuator exhibits a typical rotational motion. When the length is 11 mm, the actuator moves in a typical linear motion. The motor behavior of an actuator with a square irradiated region is shown in Supplementary Figure 7B. This means that the larger the length of the rectangular irradiated region, the more the actuator tends to move in a straight line. Furthermore, When the length of the rectangular irradiated region is constant (L = 11 mm), η_1 (length-width ratio, $\eta_1 = L/W$) only affects the motion speed of the actuator but does not affect the motion forms [Figure 4B]. It can be seen that as η_1 increases, the motion displacement of the actuator becomes smaller at the same time. The larger η_1 is, the smaller the width of the irradiated region, which means that the irradiated area of the actuator is smaller and the F_d generated is smaller under the same illumination condition, resulting in a decrease in the motion speed. Moreover, the effect of the distance between the irradiated region and the central subject on the actuator was also analyzed. As shown in Figure 4C, the irradiated region is a rectangle of 6 mm × 11 mm, and the distance h is adjusted to obtain different λ (length-distance ratio, $\lambda = L/h$). When $\lambda \geq 1$, that is, $h \leq 11$ mm, the change of h has little effect on the sliding behavior of the actuator. However, when λ is less than 1 ($h > 11$ mm), the sliding performance of the actuator has a significant decline. This may be because the increase of h improves the kinematic friction of the actuator. Therefore, the structural factors should be fully considered in the design of Marangoni effect-based actuators.

Demonstration of an integrated microrobot

As a robot that can glide on the water surface, it is more capable of performing complex work through the multifunctional integration of actuation and perception by loading function circuits. Because flexible electronics have the characteristics of light, flexible, and small, soft actuators integrated with flexible function circuits have developed vigorously in recent years[3,26-31]. In this section, we design a sensing platform that detects ambient light intensity and transmits electrical signals wirelessly to a terminal device. The circuit configurations are shown straightforward in Figure 5A, including the following: a system on a chip (SoC) with BT functionality and microcontroller unit (MCU); an analog to digital conversion (ADC) chip integrated with an operational amplifier (OPA); a photodiode (PD) with broadband response aligned to the visible region of the spectrum; a low dropout regulator and a battery providing power. The PD generates a photocurrent with a magnitude that correlates with the exposure intensity. The antenna provides a wireless interface for data extraction, causing the photoelectric signal detected by the sensing system to be displayed on the terminal device.

Based on this wireless photoelectric detection system, a structure-function integrated microrobot is designed and fabricated [Figure 5B]. The circuit board can be completely sealed against water vapor interference using encapsulated polymer (PDMS). Under laser irradiation, the integrated microrobot still exhibits controllable photo-induced sliding behavior [Figure 5C]. In previous studies, there were few robot cases that integrated functional circuits due to the lack of data on the load capacity of Marangoni effect actuators. Figure 5D provides relevant data based on the actuator in this work. A no-load actuator with a mass of 0.28 g was first manufactured. By constantly loading heavy loads until the actuator begins to sink to the bottom, the maximum load weight of the actuator is obtained at 3.05 g, which is equivalent to 1,089% of its weight. The load of the integrated actuator is 1.7 g including the encapsulation layer and the circuit board. Although the integrated microrobot can float on water, there is still a risk of sinking in the face of wind and waves. To achieve an integrated microrobot with stable floating on the surface and the ability to float from under the water to the surface, the maximum load of an actuator was obtained at 0.16 g, which is more than half its weight (57%). This means that the weight of the functional circuit system needs to be

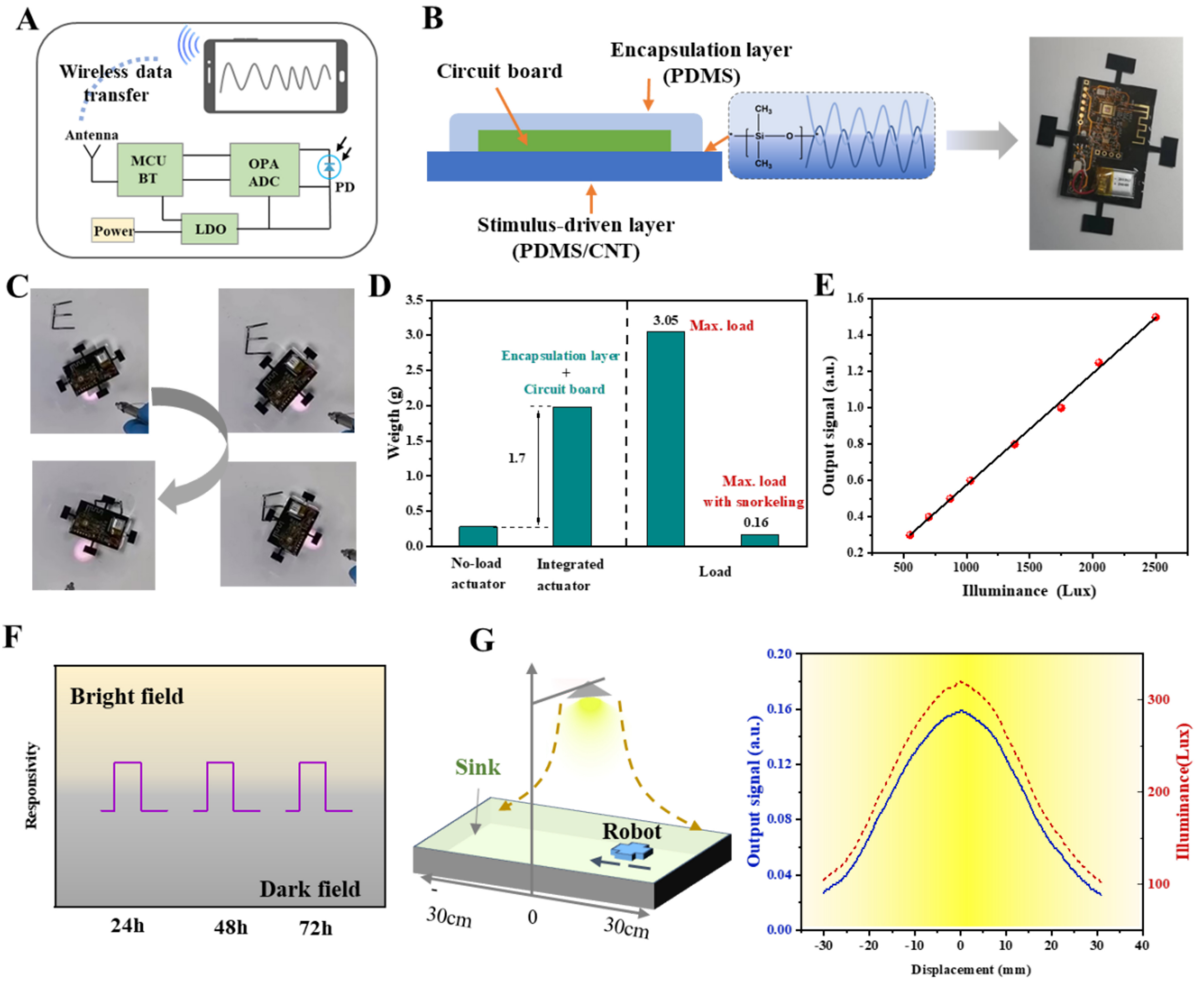

Figure 5. (A) Circuit diagram of the device and wireless communication to a terminal equipment; (B) Schematic diagram and photo of the microrobot integrated with flexible circuit; (C) Photos of the microrobot sliding on water under light action; (D) The weight and load of the actuator manufactured in this part under different conditions; (E) The linear relationship between the output signal strength of the sensing system and the luminous intensity; (F) The response of the sensing system of the microrobot to bright and dark fields under different soaking time in water; (G) A non-uniform ambient light detection diagram and results.

further reduced, which can be achieved in the future by using ultra-thin chips and other means.

For the integrated microrobot prepared in this section, the signal output strength of its photoelectric sensing system is linear with the luminous intensity [Figure 5E]. Due to the tight packaging, the sensing system of the microrobot remains photoelectric responsive after three days in water [Figure 5F], which means that the obtained actuator can perform ambient light detection tasks well. As a demonstration, a non-uniform light environment is created [Figure 5G]. As the microrobot moves from one end of the sink to the other, it is exposed to different levels of light. Based on the output signal received from the microrobot, the corresponding light intensity is easily obtained, which is of great significance for the detection of the water surface environment and the fine cultivation of aquatic organisms.

For complex detection tasks, the functions of a single microrobot may be limited, and a large-scale cluster of microrobots is more advantageous. Microrobots with different device structures and functional circuits can be designed and fabricated [Figure 6A]. Notably, the microrobot constructed in this work can be self-

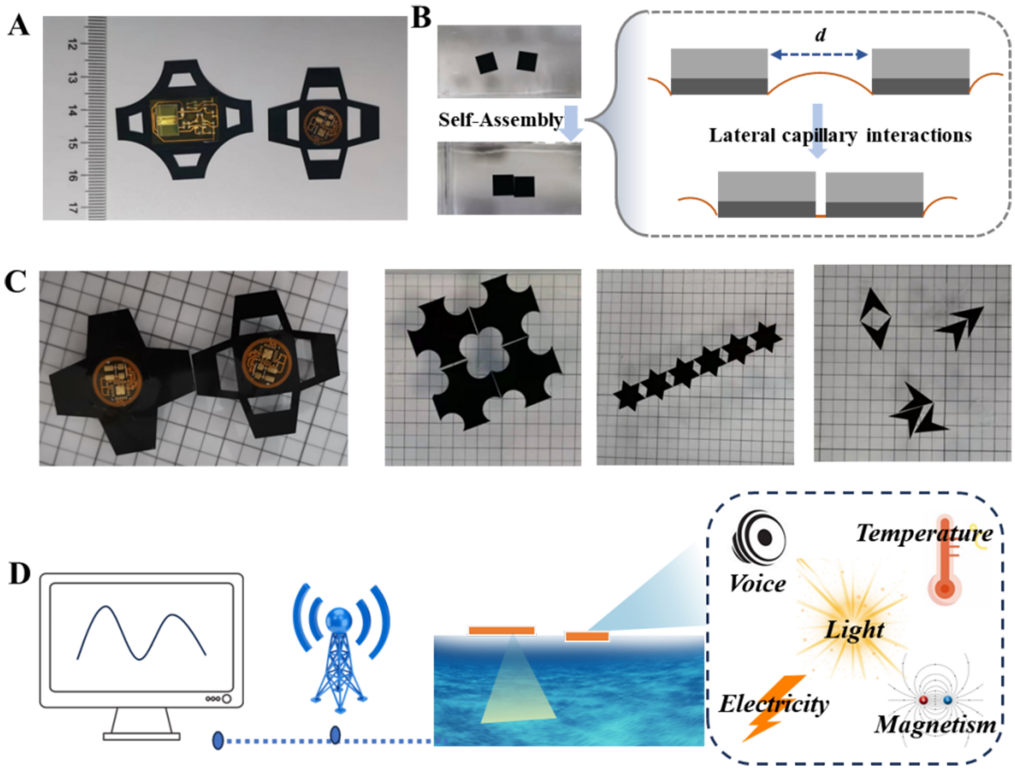

Figure 6. (A) Integrated microrobot models with different structures and circuits; (B) The self-assembly phenomenon and mechanism diagram of the microrobots on water surface. The size of the square sample is 10 mm × 10 mm; (C) Microrobot aggregates with different cluster forms generated by the self-assembly. The smallest square in the background is 5 mm × 5 mm; (D) Application scenario diagram of multi-mode information detection based on actuator cluster.

assembled in large-scale distribution [Figure 6B and C]. This is because floaters with identical wettability can self-assemble at the right distance depending on lateral capillary interaction[32,33]. The critical distance of self-assembly of the square sample in this work is about 10 mm. When the distance between two samples is less than the critical distance, they will attract each other and automatically assemble, resulting from minimization of the interfacial free energy of the liquid-liquid interface. Based on this self-assembly characteristic, microrobots with different structures can be assembled into different forms of clusters to meet the working needs [Figure 6C]. In terms of application, we have made an assumption that by distributing the integrated microrobots with different sensing systems on the target water surface, taking advantage of the cooperative operation of large-scale microrobots, a variety of environmental information can be collected [Figure 6D]. Moreover, we further compare structural parameters and properties between well-known BWSRs and this work. As shown in Supplementary Table 1, our robot showed a better parameter in terms of size and weight than those based on traditional DC motors. Although it was not as light as those actuated by piezoelectric effect, the structure-function integrated robot in this work can sense environmental information and transmit it wirelessly, which means that this kind of robot can meet diverse needs.

CONCLUSIONS

In summary, the preparation of structure-function integrated microrobots has been demonstrated for application as wireless environment detection. The structure of microrobots is derived from the PDMS/CNT actuators that can be patterned freely via laser engraving technology. The patterned floating PDMS/

CNT integrated with different wettability was fabricated for linear and rotation movements via the photothermal Marangoni effect. In particular, the motion mode and performance of the actuator can be controlled by changing the size and structure of the irradiated region in the actuator. The functionality of the microrobot is realized by the loaded wireless sensing system through the tight encapsulation of the functional platform on the actuator. The actuating PDMS/CNT substrate acts as part of the encapsulation layer to block the impact of water on the sensing system. As a result, a functional conceptual microrobot with a photoelectric detection system was demonstrated, which can detect the visible light intensity of the water surface and wirelessly transmit the data to a terminal device. Furthermore, the self-assembly behavior of these patterned robots at the water surface has been presented. It is believed that this work represents a general and promising strategy in the development of structure-function integrated microrobots with high controllability and integration.

DECLARATIONS

Authors' contributions

Conceptualization, methodology, investigation, data acquisition and analysis, and manuscript writing: Zhang, Z.
Conceptualization: Liu, L.; Zhang, F.
Methodology: Zhang, F.; Gao, N.
Investigation: Zhang, Z.; Gao, N.
Research protocol conception, overall work supervision, resource support provision, and manuscript review and editing: Chen, Y.

Availability of data and materials

All datasets generated for this study are included in the article/Supplementary Materials.

Financial support and sponsorship

This work was supported by the National Science Foundation of China, NSFC (Grant No. U20A6001) and China Postdoctoral Science Foundation (Grant Nos. 2023M733158, 2022M722822).

Conflicts of interest

Chen, Y. is an Editor on the Junior Editorial Board of the journal *Soft Science* but was not involved in any steps of the editorial process, including reviewer selection, manuscript handling, or decision-making. The other authors declare that they have no conflicts of interest.

Ethical approval and consent to participate

Not applicable.

Consent for publication

Not applicable.

REFERENCES

1. Hou, G.; Zhang, X.; Du, F.; et al. Self-regulated underwater phototaxis of a photoresponsive hydrogel-based phototactic vehicle. *Nat. Nanotechnol.* **2024**, *19*, 77-84. DOI
2. Li, G.; Chen, X.; Zhou, F.; et al. Self-powered soft robot in the Mariana Trench. *Nature* **2021**, *591*, 66-71. DOI
3. Ren, L.; Li, B.; Wei, G.; et al. Biology and bioinspiration of soft robotics: actuation, sensing, and system integration. *iScience* **2021**, *24*, 103075. DOI PubMed PMC

4. Hassani F. Bioreceptor-inspired soft sensor arrays: recent progress towards advancing digital healthcare. *Soft. Sci.* **2023**, *3*, 31. DOI
5. Kim, J. H.; Lee, S. E.; Kim, B. H. Applications of flexible and stretchable three-dimensional structures for soft electronics. *Soft. Sci.* **2023**, *3*, 16. DOI
6. Zhu, H.; Xu, B.; Wang, Y.; Pan, X.; Qu, Z.; Mei, Y. Self-powered locomotion of a hydrogel water strider. *Sci. Robot.* **2021**, *6*, eabe7925. DOI PubMed
7. Yang, X.; Chen, Y.; Zhang, X.; et al. Bioinspired light-fueled water-walking soft robots based on liquid crystal network actuators with polymerizable miniaturized gold nanorods. *Nano. Today.* **2022**, *43*, 101419. DOI
8. Jiang, J.; Tan, Q.; Yu, X.; Wu, D.; Yao, L. Research progress of bionic water strider robot. *MENG.* **2022**, *15*, 122-48. DOI
9. Yang, K.; Liu, G.; Yan, J.; Wang, T.; Zhang, X.; Zhao, J. A water-walking robot mimicking the jumping abilities of water striders. *Bioinspir. Biomim.* **2016**, *11*, 066002. DOI
10. Koh, J. S.; Yang, E.; Jung, G. P.; et al. BIOMECHANICS. Jumping on water: surface tension-dominated jumping of water striders and robotic insects. *Science* **2015**, *349*, 517-21. DOI
11. Shin, B.; Kim, H. Y.; Cho, K. J. Towards a biologically inspired small-scale water jumping robot. In *2008 2nd IEEE RAS & EMBS International Conference on Biomedical Robotics and Biomechatronics*, Scottsdale, USA, Oct 19-22 2008; IEEE, 2008. pp 127-31. DOI
12. Okawa, D.; Pastine, S. J.; Zettl, A.; Fréchet, J. M. Surface tension mediated conversion of light to work. *J. Am. Chem. Soc.* **2009**, *131*, 5396-8. DOI PubMed PMC
13. Wu, H.; Chen, Y.; Xu, W.; et al. High-performance Marangoni hydrogel rotors with asymmetric porosity and drag reduction profile. *Nat. Commun.* **2023**, *14*, 20. DOI PubMed PMC
14. Wang, X.; Dai, L.; Jiao, N.; Tung, S.; Liu, L. Superhydrophobic photothermal graphene composites and their functional applications in microrobots swimming at the air/water interface. *Chem. Eng. J.* **2021**, *422*, 129394. DOI
15. Rich, S. I.; Wood, R. J.; Majidi, C. Untethered soft robotics. *Nat. Electron.* **2018**, *1*, 102-12. DOI
16. Heng, W.; Solomon, S.; Gao, W. Flexible electronics and devices as human-machine interfaces for medical robotics. *Adv. Mater.* **2022**, *34*, e2107902. DOI PubMed PMC
17. Jin, J.; Wang, S.; Zhang, Z.; Mei, D.; Wang, Y. Progress on flexible tactile sensors in robotic applications on objects properties recognition, manipulation and human-machine interactions. *Soft. Sci.* **2023**, *3*, 8. DOI
18. Iyer, V.; Gaensbauer, H.; Daniel, T. L.; Gollakota, S. Wind dispersal of battery-free wireless devices. *Nature* **2022**, *603*, 427-33. DOI PubMed
19. Wehner, M.; Truby, R. L.; Fitzgerald, D. J.; et al. An integrated design and fabrication strategy for entirely soft, autonomous robots. *Nature* **2016**, *536*, 451-5. DOI
20. Jafferis, N. T.; Helbling, E. F.; Karpelson, M.; Wood, R. J. Untethered flight of an insect-sized flapping-wing microscale aerial vehicle. *Nature* **2019**, *570*, 491-5. DOI PubMed
21. Gao, A.; Butt, H. J.; Steffen, W.; Schönecker, C. Optical manipulation of liquids by thermal marangoni flow along the air-water interfaces of a superhydrophobic surface. *Langmuir* **2021**, *37*, 8677-86. DOI PubMed PMC
22. Wang, W.; Han, B.; Zhang, Y.; et al. Laser-induced graphene tapes as origami and stick-on labels for photothermal manipulation via marangoni effect. *Adv. Funct. Mater.* **2021**, *31*, 2006179. DOI
23. Yong, J.; Chen, F.; Yang, Q.; et al. Controllable adhesive superhydrophobic surfaces based on PDMS microwell arrays. *Langmuir* **2013**, *29*, 3274-9. DOI
24. Whyman, G.; Bormashenko, E.; Stein, T. The rigorous derivation of Young, Cassie–Baxter and Wenzel equations and the analysis of the contact angle hysteresis phenomenon. *Chem. Phys. Lett.* **2008**, *450*, 355-9. DOI
25. Yang, Y.; Bai, H.; Li, M.; et al. An interfacial floating tumbler with a penetrable structure and Janus wettability inspired by *Pistia stratiotes*. *Mater. Horiz.* **2022**, *9*, 1888-95. DOI
26. Zhang, Z.; Yu, Y.; Yu, H.; Feng, Y.; Feng, W. Water-resistant conductive organogels with sensation and actuation functions for artificial neuro-sensory muscular systems. *SmartMat* **2022**, *3*, 632-43. DOI
27. Chen, Y.; Zhang, Y.; Liang, Z.; Cao, Y.; Han, Z.; Feng, X. Flexible inorganic bioelectronics. *npj. Flex. Electron.* **2020**, *4*, 65. DOI
28. Zhang, Z.; Zhang, F.; Jian, W.; Chen, Y.; Feng, X. Photothermal-responsive lightweight hydrogel actuator loaded with polydopamine-modified hollow glass microspheres. *ACS. Appl. Mater. Interfaces.* **2024**, *16*, 23914-23. DOI
29. Lin, Y.; Siddall, R.; Schwab, F.; et al. Modeling and control of a soft robotic fish with integrated soft sensing. *Adv. Intell. Syst.* **2023**, *5*, 2000244. DOI
30. Bang, J.; Choi, S. H.; Pyun, K. R.; et al. Bioinspired electronics for intelligent soft robots. *Nat. Rev. Electr. Eng.* **2024**, *1*, 597-613. DOI
31. Qu, J.; Cui, G.; Li, Z.; et al. Advanced flexible sensing technologies for soft robots. *Adv. Funct. Mater.* **2024**, *34*, 2401311. DOI
32. Bowden, N.; Terfort, A.; Carbeck, J.; Whitesides, G. M. Self-assembly of mesoscale objects into ordered two-dimensional arrays. *Science* **1997**, *276*, 233-5. DOI PubMed
33. Grzybowski, B. A.; Bowden, N.; Arias, F.; Yang, H.; Whitesides, G. M. Modeling of menisci and capillary forces from the millimeter to the micrometer size range. *J. Phys. Chem. B.* **2001**, *105*, 404-12. DOI